Supplementary Materials to:

3D-printed flow-mode atmospheric pressure glow discharge reactor for the synthesis of multi-metallic Pt-/ Pd-/ Os-/ Ru-/ Re-/ W-/ Cr-/ nanocluster catalysts

Angelika Nowak[a*], Piotr Jamroz[a], Mateusz M. Marzec[b], Krystian Sokolowski[b], Anna Dzimitrowicz[a], Paweł Pohl[a], Andrzej Bernasik[b,c], Piotr Cyganowski[d*]

[a]*Department of Analytical Chemistry and Chemical Metallurgy, Wroclaw University of Science and Technology, Wybrzeze St. Wyspianskiego 27, 50-370 Wroclaw, Poland*

[b]*Academic Centre for Materials and Nanotechnology, AGH University of Krakow, A. Mickiewicza 30, 30-059 Krakow, Poland*

[c]*Faculty of Physics and Applied Computer Science, AGH University of Krakow, A. Mickiewicza 30, 30-059 Krakow, Poland*

[d]*Department of Process Engineering and Technology of Polymer and Carbon Materials, Wroclaw University of Science and Technology, Wybrzeze St. Wyspianskiego 27, 50-370 Wroclaw, Poland*

*Corresponding authors: Angelika Nowak (angelika.nowak@pwr.edu.pl) and Piotr Cyganowski (piotr.cyganowski@pwr.edu.pl)

S1. Detailed Methods and Materials

S1.1 Plasma reactor design

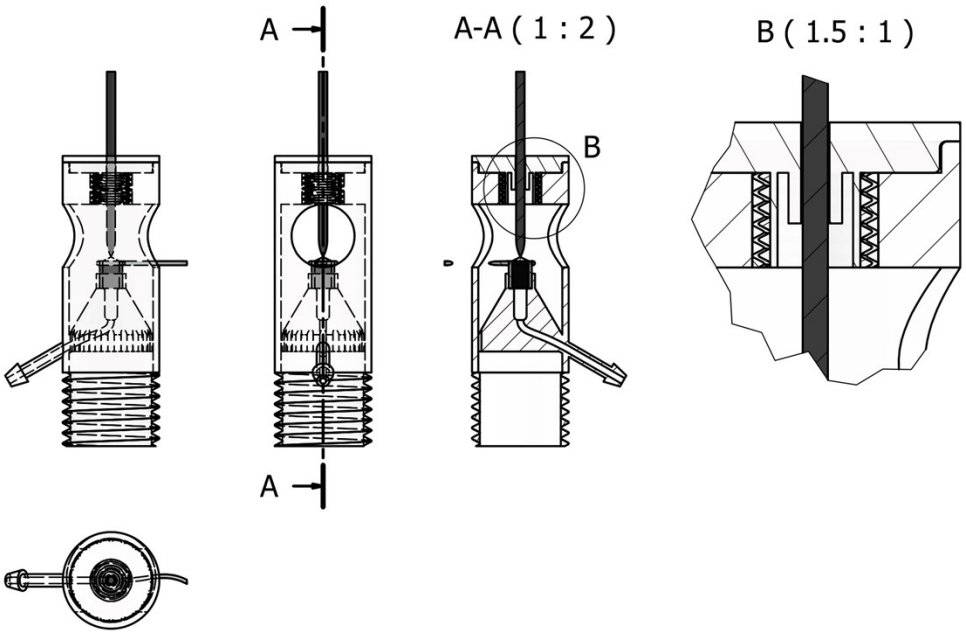

Figure S1. Technical presentation of the applied CAPP system.

Table S1. Current-voltage parameters used for nanocluster catalysts (NCs) synthesis by flowing liquid anode direct-current atmospheric pressure glow discharge (FLA-dc-APGD) and flowing liquid cathode direct-current atmospheric pressure glow discharge (FLC-dc-APGD).

	FLA-dc-APGD		FLC-dc-APGD	
Synthesized NCs	**Voltage [V]**	**Current [mA]**	**Voltage [V]**	**Current [mA]**
$\mathbf{Pt^{Os}}$	1230	40	1150	46
$\mathbf{Os^{Pd/Cr}}$	1360	55	1160	58
$\mathbf{Ru^{W}}$	1350	52	1110	46
$\mathbf{W^{Ru/Os}}$	-*	-*	1110	46
$\mathbf{Re^{Os}}$	1300	46	-*	-*

*The plasma was unstable, therefore the synthesis was not performed

S1.2 Reagents and solutions

The reagents used for the NCs synthesis containing Os(IV), Ru(III), Re(VII), W(VI), and Cr(VI) solutions were obtained from Sigma Aldrich (USA), while for Pt(IV), and Pd(II) from Innovator (Poland). The precursor solution of 1000 mg L^{-1} Pt(IV) ions stock solution was prepared from H_2PtCl_6 (30% solution). The ruthenium precursor solution was a 1000 mg L^{-1} stock solution of Ru(III) ions, prepared using $RuCl_3$, while $(NH_4)_2OsCl_6$ and $Na_2WO_4 \cdot 2H_2O$ reagent were used to 1000 mg L^{-1} Os(IV) and 1000 mg L^{-1} W(VI), respectively ions stock solution preparation. Moreover 1000 mg L^{-1} Re(VII) solution was prepared using NH_4ReO_4 and 1000 mg L^{-1} Pd(II) solution using H_2PdCl_4. The potassium dichromate ($K_2Cr_2O_7$) solution of 1000 mg L^{-1} Cr(VI) was also prepared. Sodium tetrahydroborate (THB) and 4-nitrophenol (4-NP) for catalytic activity analysis were acquired from Sigma-Aldrich (USA). These solutions were freshly prepared in water.

S1.3 Characterization of NCs

The size distribution, hydrodynamic diameter (D_h) and polydispersity index (PdI) of NCs synthesized by FLA-dc-APGD and FLC-dc-APGD were evaluated using dynamic light scattering (DLS) at temperature of 20°C. Samples were measured in 1-cm polystyrene cuvette. Zeta potential (ξ) and conductivity (σ) of the NCs synthesized by FLA-dc-APGD and FLC-dc-APGD were

examined by electrophoretic light scattering (ELS), to assess samples stability, focusing on aggregation and changes in surface charge. Ru^{W}NCs synthesized by FLA-dc-APGD and FLC-dc-APGD were diluted tenfold prior to measurements. The evaluation was taken in polycarbonate Omega cuvette at temperature of 25°C. A Litesizer 500 device (Anton Paar GmbH, Austria) was utilized for this purpose, while the obtained data were analyzed using Kalliope software (Anton Paar, Austria).

The concentrations of metals in NCs catalysts were determined using inductively coupled plasma optical emission spectrometry (ICP-OES) using an Agilent 5110 instrument. The optical characteristics of the NCs synthesized by FLA-dc-APGD and FLC-dc-APGD techniques were evaluated through UV/Vis absorption spectrophotometry utilizing the SPECORD 210 PLUS spectrophotometer (Analytik Jena, Jena AG, Germany). Absorption spectra were recorded across the wavelength range of 190 to 1100 nm with a spectral resolution of 1 nm using 1-cm quartz cuvette.

The structural characterization of NCs was performed using a TITAN^3 G^2 60-300 high-resolution transmission electron microscope HRTEM (FEI Company, now Thermo Fisher Scientific) with selected area electron diffraction (SAED), energy-dispersive X-ray spectroscopy (EDX) and a high-angle annular dark-field (HAADF) detector. The resulting NCs solutions were placed onto Cu grids (100 mesh, Agar Scientific Ltd., Stansted, Great Britain) and evaporated in air atmosphere. High-resolution TEM images were analyzed using ImageJ 1.54 (National Institutes of Health, Bethesda, MD, USA) software to create histograms representing the average size distribution of observed nanoclusters.

S1.4 Catalytic activity studies

The study of the catalytic activity of the obtained NCs, synthesized by using dc-APGD was based on the model reaction with 4-NP. Reaction with 4-NP evaluate the catalytic performance of the NCs, moving in the direction of 4-aminophenol (4-AP) formation, with a catalyst being necessary for the reaction to proceed. UV-Vis measurements (Specord 210 Plus, Analytik Jena, Germany) in a 3 mL quartz cuvette were used to monitor NCs catalytic activity. The measurement procedure was performed by recording the spectrum of 2.5 mL of a 4-NP solution (0.1 mmol L^{-1}). The spectrum revealed a distinct absorption band of 4-NP at λ_{max} = 318 nm. Adding 0.3 mL of a $NaBH_4$

solution (0.1 mol L^{-1}) to measured 4-NP moved the absorption band to λ_{max} = 400 nm, indicating the production of the 4-nitrophenolate anion [1]. Finally, 0.1 mL or 0.01 mL of the suspension of NCs in depending of the sample was added to the cuvette, and the spectra in the 200-600 nm spectra range were recorded. Afterwards, the change in absorbance at 400 nm occurred because of the initiation and continuation of the reduction from 4-NP to 4-AP. The obtained absorbances were then utilized to simulate the pseudo-first order kinetics of the reaction. Therefore the experiment was set in such a way that there was a significant excess of $NaBH_4$ in the reaction. According to the Lambert-Beer law, it was thought that the ratio of NCs concentrations equals the ratio of their absorbances. Based on the proportionality between concentration and absorbance for the 4-nitrophenolate anion, a plot of $-\ln(A_t/A_0)$ versus time (t) was generated, with A_t being the absorbance at time t and A_0 the absorbance at the start of the reaction. The pseudo-first order rate constant ($k_1{}^b$ in min^{-1}) and mass normalized rate constant ($k_{1m}{}^b$ in $min^{-1}mg^{-1}$) were calculated from the slopes of the resulting plots.

To evaluate the efficiency of the catalyst in promoting the conversion of 4-NP to 4-AP, turnover frequency (TOF) which represents the changing conversion percentage (%) of 4-NP over time was calculated, as described Khan et al. [1]. To assess the molar activity of the Pt^{Os}NCs, $Os^{Pd/Cr}$NCs, Ru^{W}NCs, $W^{Ru/Os}$NCs, and Re^{Os}NCs TOFs parameter values were calculated utilizing equation (S1):

$$TOF = n_{4-NP} * r * n_{NCs}^{-1} * t^{-1} \quad (S1)$$

where n_{4-NP} and n_{NCs} represent the number of moles of 4-NP and NCs, respectively, whereas t stands for the reaction time (in mins), and r corresponds to the yield (%) of the reduction process.

S1.5 XPS analysis

X-ray Photoelectron Spectroscopy (XPS) analyses were conducted using a PHI VersaProbe II Scanning XPS system equipped with a monochromatic Al Kα radiation source (hν = 1486.6 eV). The X-ray beam was focused to a 100 μm spot and rastered over a 400 × 400 μm^2 area to ensure representative sampling. Spectra were collected at a photoelectron take-off angle of 45° with a pass energy of 46.95 eV and an energy step size of 0.1 eV, providing high-resolution data for the analyzed core levels regions. A dual-beam charge neutralization system, combining 7 eV Ar^+ ions and 1 eV electrons, was employed to stabilize the surface potential during measurements. All

binding energies were calibrated against the C-C component of the C 1s peak at 285.0 eV. The pressure in the analysis chamber was maintained below 4×10^{-9} mbar throughout the measurements. Peak fitting and quantitative analysis were performed using PHI MultiPak software (version 9.9.3). High-resolution XPS spectra were fitted using mixed Gaussian–Lorentzian line shapes (with the Lorentzian contribution limited to 25%), following background subtraction using the Shirley method. For spin–orbit split components (p, d, and f), the peak area ratios were constrained to the theoretical values of 2:1, 3:2, and 4:3, respectively, while the energy separations were fixed according to reference data. The full width at half maximum (FWHM) values were maintained within physically reasonable and consistent ranges for analogous spectral components, except where chemical state dependent broadening or narrowing was expected. Based on the instrument geometry, the information depth of the measurements was estimated to be approximately 5 nm. For the XPS analysis, the solutions containing Pt^{Os}NCs, $Os^{Pd/Cr}$NCs, Ru^{W}NCs, $W^{Ru/Os}$NCs, and Re^{Os}NCs were repeatedly drop-cast and evaporated onto silicon wafer substrates.

S2. Detailed Results and Discussion

S2.1 NCs characteristic

The size by number results (Figure 2) indicate a variation in particle diameter as a consequence of cold atmospheric pressure plasma (CAPP) treatment. In the case of Pt, the application of FLA-dc-APGD and FLC-dc-APGD resulted in formation of Pt^{Os}NCs with average particle diameter of 190.0±2.9 nm and 320.0±4.7 nm, respectively. Conversely, $Os^{Pd/Cr}$NCs exhibited a significantly larger average particle diameter of 3017.7±74.9 nm following FLA-dc-APGD and further to 131.2±2.1 nm after FLC-dc-APGD treatment. In the case of Ru^{W}NCs, the response to plasma treatment with FLA-dc-APGD resulting in 275.9±4.1 nm, and in case of FLC-dc-APGD it was 1416.0±42.3 nm. For Re^{Os}NCs, the particle size was 134.1±3.4 nm after FLA-dc-APGD treatment, and 110.7±2.8 nm for $W^{Ru/Os}$NCs upon application of FLC-dc-APGD. A notable increment in average particle size distribution indicates that, upon exiting the plasma zone, individual particles tend to form larger agglomerates, which are subsequently detected and classified as larger particles by DLS device [2]. Particles within the plasma phase undergo interactions with dc-APGD derived reactive species. In non-thermal plasmas, the high electron

temperature and mobility lead to a predominance of electron-particle collisions. This results in the accumulation of negative charge on the particle surfaces, which effectively suppresses particle agglomeration. The selective plasma heating, driven predominantly by the recombination of ions or radicals at the particle surface, leads to a particle temperature exceeding that of the ambient plasma gas, facilitating crystallization processes [3]. As reported by Cui et al. [4], platinum nanoparticles (PtNPs) with particle size down to 2 nm can be synthesized by microwave discharge plasma, which contrasts with the values obtained in this study. However, there is currently a lack of published studies focusing on the synthesis of OsNCs by CAPP, highlighting a significant gap in the existing nanomaterials research. Nonetheless, literature reports information about OsNPs synthesis by irradiation with electrons, yielding particles with a size ranging of 1.5 to 50 nm [5]. Following this, RuNPs synthesized by glow discharge [6] can be characterized by a narrow size distribution within the 1-2 nm range. Similarly, Müller et al. [2] reported substantially smaller particle sizes for WNPs, with diameters as low as 12 nm obtained by a radio-frequency (rf) dielectric barrier discharge in form of plasma jet. Such variations between literature and our research may be attributed to differences in synthesis conditions such as a precursor chemical compound and concentration, plasma type and process parameters.

Optical properties of NCs synthesized by CAPP were investigated by UV/Vis absorption spectrophotometry. As shown in Figure S1, the UV/Vis spectra of Pt^{Os}NCs, $Os^{Pd/Cr}$NCs, and Ru^{W}NCs synthesized by FLA-dc-APGD and FLC-dc-APGD remain relatively unchanged. The only evident difference is the increased absorbance values for the Pt^{Os}NCs and $Os^{Pd/Cr}$NCs synthesized by FLA-dc-APGD in comparison to those obtained by FLC-dc-APGD.

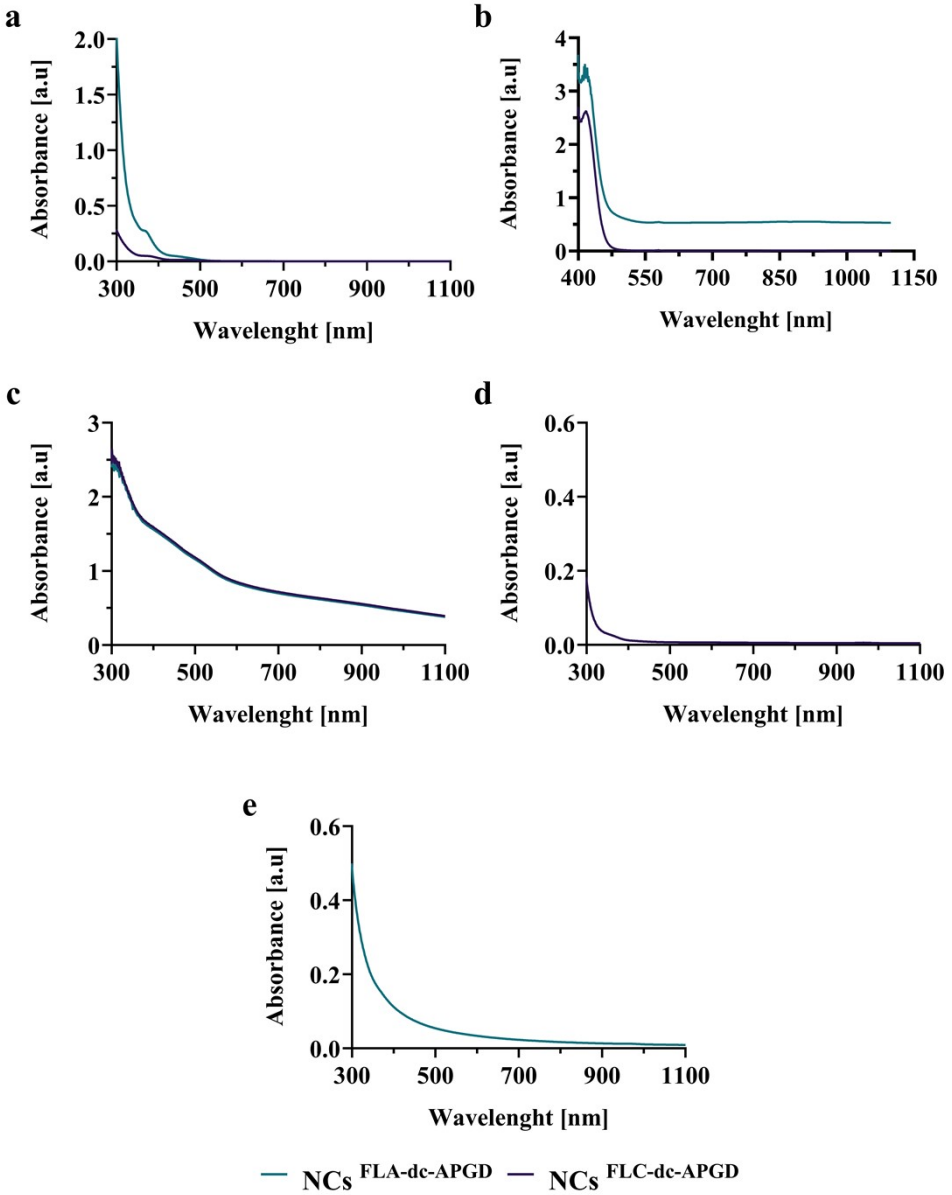

160

161 **Figure S2.** The UV/Vis spectra for NCs synthesized by FLA-dc-APGD and FLC-dc-APGD for Pt^{Os}NCs
162 (a), $Os^{Pd/Cr}$NCs (b), Ru^{W}NCs (c), $W^{Ru/Os}$NCs (d), and Re^{Os}NCs (e), where, exceptionally, the Ru^{W}NCs
163 analysis was conducted on solutions diluted 10 times.

164 The assessed PdI value of the analyzed NCs suggest uniform size distribution (see Table
165 S2), with the most close monodisperse population observed for $Os^{Pd/Cr}$NCs synthesized by FLA-
166 dc-APGD. As it was observed before NPs of varying sizes and/or velocities can exhibit different
167 probabilities of becoming charged by the CAPP [7]. Additionally, in nonstationary plasmas, bipolar
168 charge distributions can lead to attractive Coulomb forces that enhances coagulation process [8], and

therefore resulting in a broader size distribution. In addition, the spherical morphology of NPs can be achieved through the addition of stabilizing agent [9]. Data regarding the PdI of NPs synthesized by CAPP are not reported in the available literature, however PdI values for NPs obtained through alternative synthesis methods are documented. Previous studies have demonstrated that highly monodisperse laser-generated PtNPs with a PdI of 0.05 can be achieved by using downstream centrifugation [10]. Additionally, a PdI=0.18 has been reported for PtNPs synthesized using plant-based analytes present in the extract of *Sechium edule* [11]. Unfortunately, no PdI values for OsNPs have been provide. El-Sayed et al. [12] demonstrated a PdI value for imidazolium ionic liquid coated RuNPs implies uniformity in NPs size (PdI=0.23), suggesting efficient control over the synthesis process. For WO_3 NPs, a PdI of 0.22 can be achieved through biogenic synthesis employing the Taguchi method [13]. Details regarding D_h values can be found in the Table S2.

Table S2. Polydispersity index (PdI) and mean hydrodynamic diameter (D_h) of NCs synthesized by FLA-dc-APGD and FLC-dc-APGD.

	NCs synthesized by FLA-dc-APGD		**NCs synthesized by FLC-dc-APGD**	
Sample	PdI [%]	D_h [nm]	PdI [%]	D_h [nm]
Pt^{Os}NCs	24.0	1921.4	28.3	608.3
$Os^{Pd/Cr}$NCs	16.3	3547.1	29.6	647.3
Ru^{W}NCs	31.8	2599.2	27.7	3189.3
$W^{Ru/Os}$NCs	-*	-*	21.6	271.1
Re^{Os}NCs	23.7	174.4	-*	-*

*The synthesis was not performed in this study

NCs stability is determined by the ξ value, as it indicates the extent of interparticle electrostatic repulsion [14]. The measured ξ (Table 1) for the Pt^{Os}NCs and $Os^{Pd/Cr}$NCs synthesized by FLA-dc-APGD and FLC-dc-APGD suggest colloidal instability. In contrast, the Ru^{W}NCs, $W^{Ru/Os}$NCs, and Re^{Os}NCs indicated improved dispersion stability. This was evidenced by ξ values approaching ±30 mV, a range typically associated with sufficient electrostatic repulsion to prevent particle aggregation [15]. Throughout the CAPP treatment, plasma-generated ions are directed toward the substrate surface, initiating bombardment that triggers a range of surface-related modifications. An example of this interaction is the formation of hydrophilic functional groups,

191 which is additionally influenced by the characteristics of the treated substrate [16]. Moreover, CAPP
192 treatment results in the generation of reactive oxygen and nitrogen species (RONS), which modify
193 the NPs surface also through the introduction of new functional groups. According to findings
194 presented by Zhao et al. [17], CAPP treatment time can impact the stability of NPs by modifying
195 their surface charge. In the case of PtNPs, extension of sample treatment time by plasma jet from
196 2 to 5 mins resulted in a ξ change from -56.0 mV to -12.5 mV [17]. A review of the available literature
197 reveals a lack of reported ξ for OsNCs and RuNCs synthesized by CAPP. An example involving
198 WNPs includes WO_3 synthesized by underwater impulse discharge, which demonstrate a zeta
199 potential of approximately -30 mV [18].

200 The differences in σ arise from the application of CAPP as well as from the precursors
201 employed. Specifically, change in conductivity value can be attributed to the presence of RONS
202 generated within the plasma environment [19]. These reactive species are known to interact with the
203 surface, potentially inducing surface modifications [20], thereby resulting in improved electrical
204 conductivity of NCs.

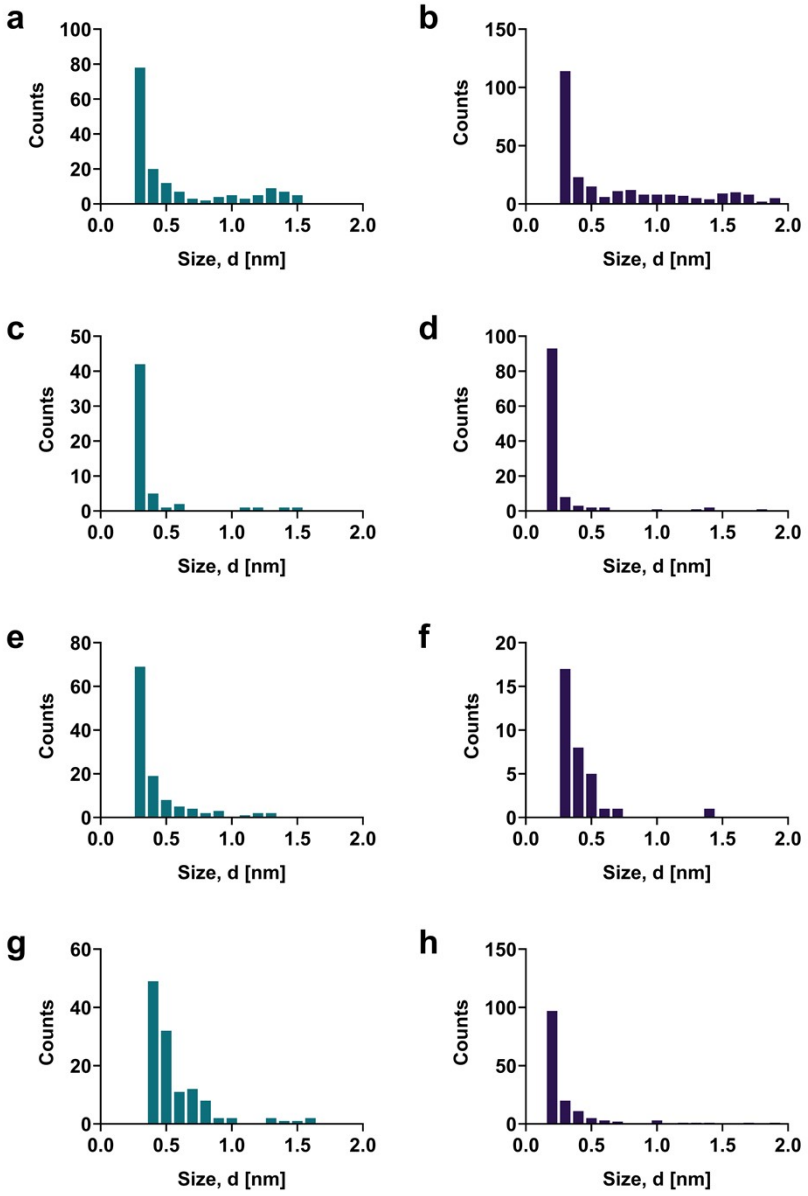

205

206 **Figure S3.** Size distribution from HRTEM of $Pt^{Os}NCs^{FLA\text{-}dc\text{-}APGD}$ (a), $Pt^{Os}NCs^{FLC\text{-}dc\text{-}APGD}$ (b),
207 $Os^{Pd/Cr}NCs^{FLA\text{-}dc\text{-}APGD}$ (c), $Os^{Pd/Cr}NCs^{FLC\text{-}dc\text{-}APGD}$ (d), $Ru^{W}NCs^{FLA\text{-}dc\text{-}APGD}$ (e), $Ru^{W}NCs^{FLC\text{-}dc\text{-}APGD}$
208 (f), and $Re^{Os}NCs^{FLA\text{-}dc\text{-}APGD}$ (g), and $W^{Ru/Os}NCs^{FLC\text{-}dc\text{-}APGD}$ (h).

209 **Table S3.** ICP-OES results related to the NC catalysts. Mean element concentrations (in mg L^{-1}) with standard deviations (n=3)

210

Sample	Os	Pd	Pt	Re	Ru	W	Cr
Pt^{Os}NCs (FLC)	1,2±0,4	<2,2	58,4±0,4	<1,5	<0,5	<1,3	<0,5
Ru^{W}NCs (FLC)	<0,5	<2,2	<1,1	<1,5	392,7±7,9	6,9±1,1	<0,5
Ru^{W}NCs (FLA)	<0,5	<2,2	<1,1	<1,5	369,8±1,7	6,0±0,2	<0,5
$W^{Ru/Os}$NCs (FLC)	0,9±0,1	<2,2	<1,1	<1,5	9,9±0,1	1094,5±6,5	<0,5
$W^{Ru/Os}$NCs (FLA)	4,3±0,1	<2,2	<1,1	20,4±0,8	<0,5	<1,3	<0,5
Re^{Os}NCs (FLC)	<0,5	<2,2	<1,1	755,5±3,2	<0,5	2,9±1,2	<0,5
Re^{Os}NCs (FLA)	5,3±2,2	1292,9±12,2	<1,1	<1,5	<0,5	<1,3	<0,5
Pd^{Os}NCs (FLC)*	0,7±0,1	1292,5±4,3	<1,1	<1,5	<0,5	<1,3	<0,5
Pd^{Os}NCs (FLA)*	1,7±0,5	<2,2	<1,1	708,8±2,4	<0,5	2,4±0,2	<0,5
$Os^{Pd/Cr}$NCs (FLC)	454,4±4,2	5,5±0,8	<1,1	<1,5	<0,5	<1,3	1,3±0,1

* Sample not included into the manuscript

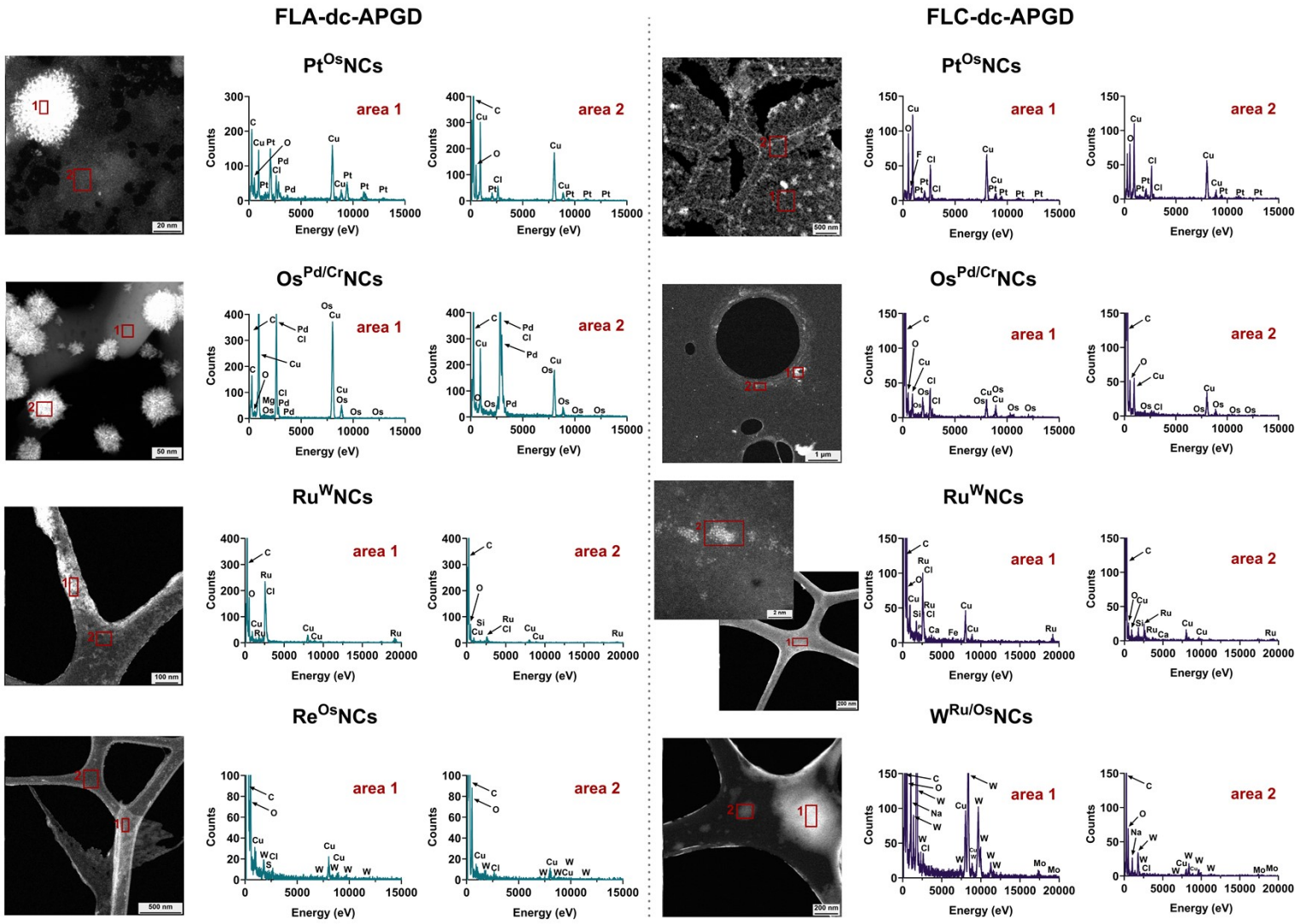

212

213 **Figure S4.** HRTEM photomicrographs and EDX spectra of NCs synthesised by FLA-dc-APGD and FLC-dc-APGD. Each panel presents
214 photomicrograph and corresponding EDX spectra of the highlighted HRTEM areas.

S2.2 Catalytic reaction

An initial NCs volume of 100 µL was employed in the experiment. However, in the case of Ru^{W}NCs synthesized by FLA-dc-APGD and FLC-dc-APGD, this volume proved unsuitable due to the excessively rapid reaction rate (catalyst mass= 0.0638 mg), which resulted in a rapid flattening of the UV/Vis spectrum at 400 nm and prevented reliable kinetic analysis. Therefore, additional experiments were conducted using different NCs volumes to identify appropriate volume that still enabled accurate monitoring of the reaction progress as is presented in Figure S5. This approach also enabled plotting of a first-order kinetic plot with a linear dependance, allowing the determination of the reaction rate over the entire measured range. For Ru^{W}NCs, a catalyst mass of 0.000637 mg was applied, as shown in Figure S5, as well as a mass of 0.00637 mg, presented in Figure 5. The use of the higher catalyst mass resulted in a more uniform first-order kinetic profile (see Figure 5). Accordingly, finally two distinct NCs volumes (100 µL for Pt^{Os}NCs, $Os^{Pd/Cr}$NCs, $W^{Ru/Os}$NCs, Re^{Os}NCs and 10 µL for Ru^{W}NCs) were applied, necessitating the calculation of $k_{1m}{}^{b}$, which are provided in Table 2.

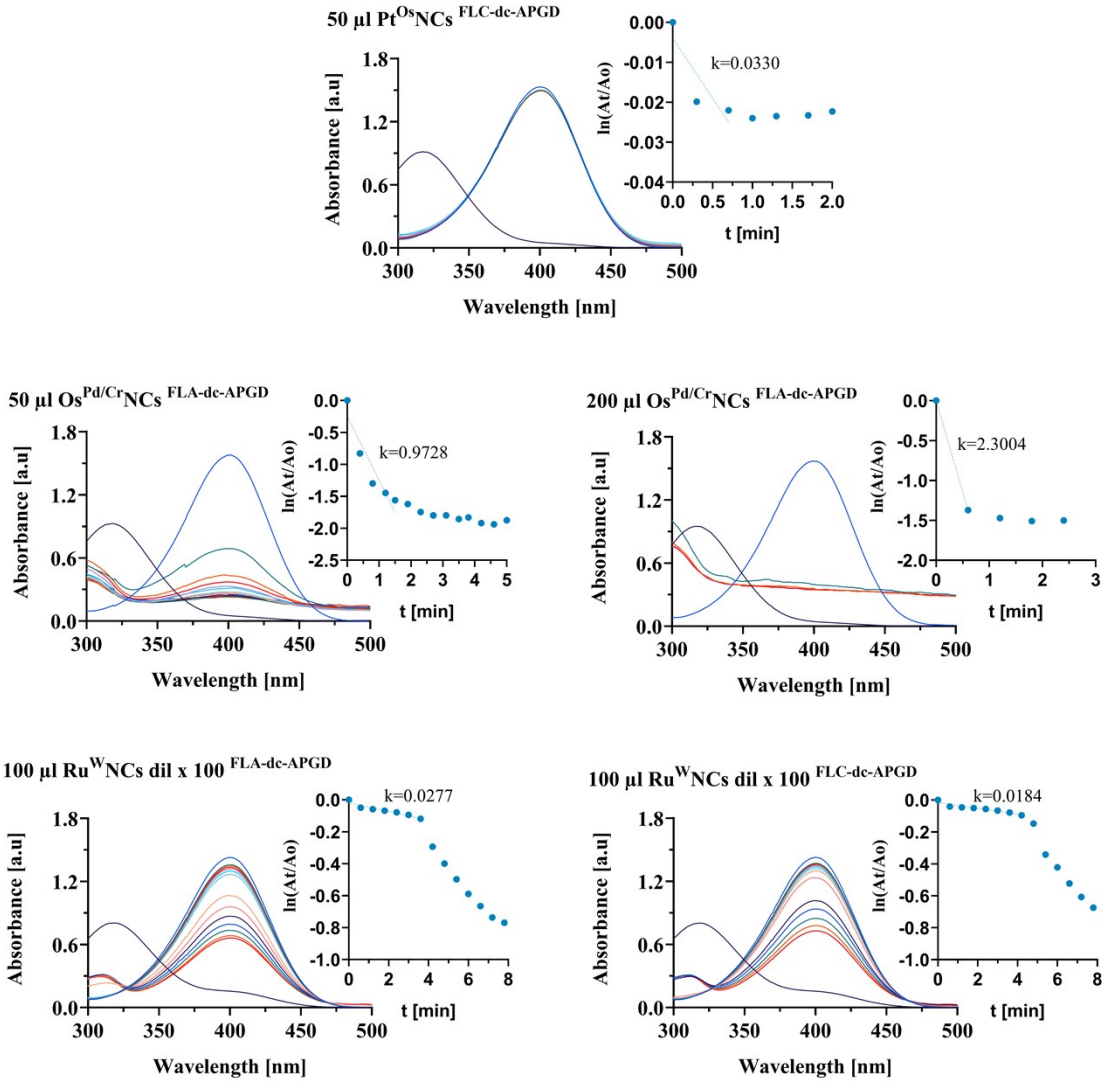

229

230 **Figure S5.** UV/Vis absorption spectra and first-order kinetic plots for the reduction of 4-NP using selected
231 NCs synthesised by FLA-dc-APGD or FLC-dc-APGD at different catalyst volumes to determine the
232 appropriate catalyst amount.

233 Calculated TOF value represents the number of catalytic reactions occurring per active site
234 over time. The values of the TOFs for 20, 40, 60, 80 and 100% 4-NP conversions are displayed in
235 Figure S2. The TOF values for all samples exhibited a decline as the extent of reduction
236 approached its maximum. The $Os^{Pd/Cr}$NCs and Ru^{W}NCs synthesized by FLA-dc-APGD reveal the
237 greatest values of TOF of 0.76, and 0.89 min^{-1} for 20%, and 0.37, and 0.27 min^{-1} for 100% of 4-
238 NP conversion, respectively. Conversely, the lowest activities were observed for $W^{Ru/Os}$NCs and
239 Re^{Os}NCs. It can be observed that the TOF values obtained for NCs synthesized via FLA-dc-APGD

were approximately at least two times higher in the case of Pt^{Os}NCs, and $Os^{Pd/Cr}$NCs in comparison to those NCs synthesized by FLC-dc-APGD. In contrast, for Ru^{W}NCs, the TOF values for catalysts synthesized by both FLA-dc-APGD and FLC-dc-APGD were almost comparable, for instance, the TOF at 100% conversion was 0.27 min^{-1} and 0.24 min^{-1}, respectively. This suggests a greater availability of $Os^{Pd/Cr}$NCs and Ru^{W}NCs synthesized by FLA-dc-APGD, what is in pair with catalytic activity results (see Table 2).

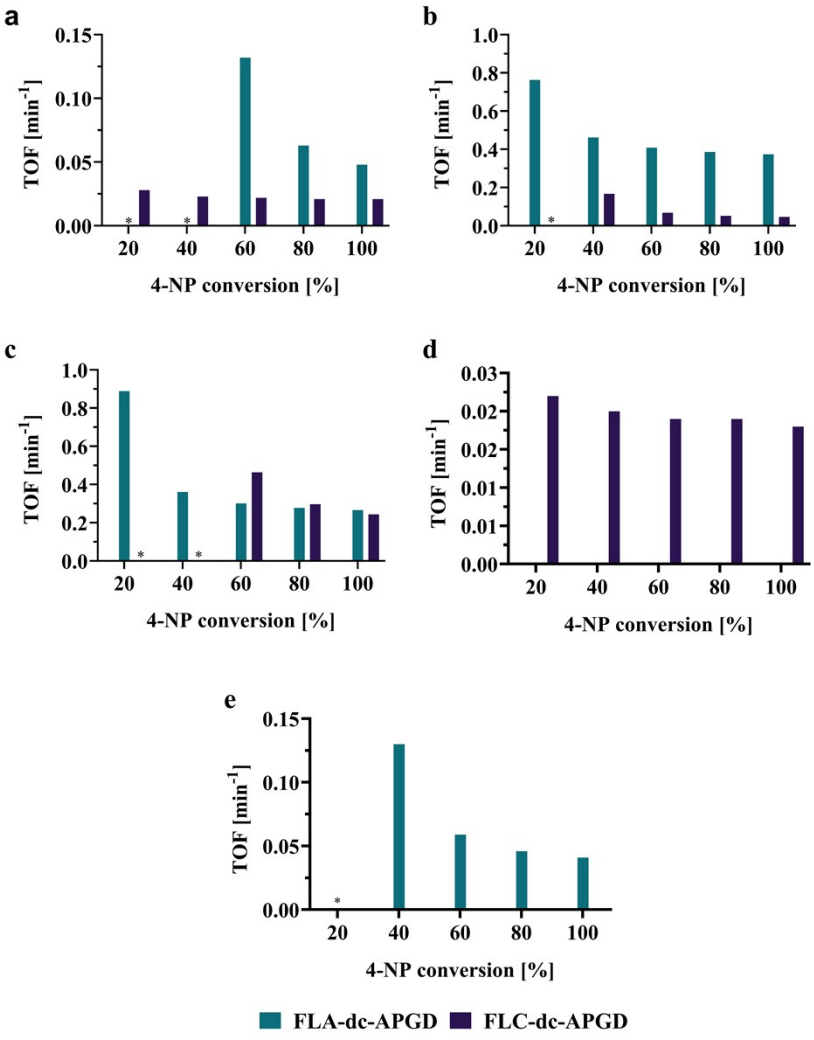

Figure S6. The TOFs for 20, 40, 60, 80%, and 100% 4-NP conversions for NCs synthesized by FLA-dc-APGD and FLC-dc-APGD for Pt^{Os}NCs (a), $Os^{Pd/Cr}$NCs (b), Ru^{W}NCs (c), $W^{Ru/Os}$NCs (d), and Re^{Os}NCs (e), where * means that the TOF value can not be determined because after introducing the catalyst into the reaction the degree of conversion was already higher than the range assumed in the graph.

S2.3 Oxidation states of d-block elements in NCs morphology

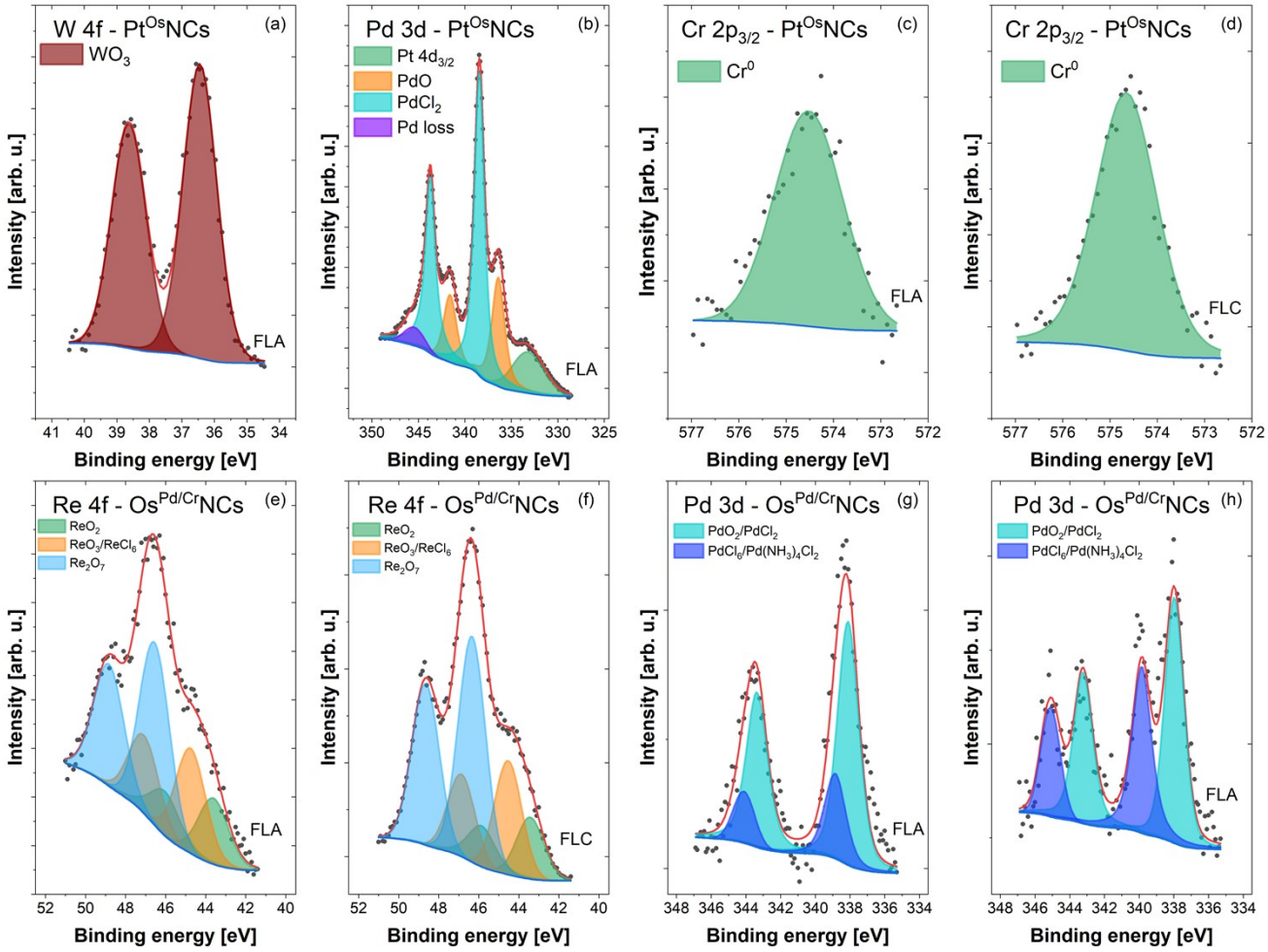

252

253 **Figure S7.** High-resolution XPS spectra of the main core level lines in the Pt^{Os}NCs (a,b,c,d) and $Os^{Pd/Cr}$NCs (e,f,g,h) samples.

Table S4. Surface compositions (atomic %) determined by fitting XPS spectra for Pt^{Os}NCs synthesized by FLA-dc-APGD and FLC-dc-APGD.

Element	**C**			**N**		**O**	**Cl**	**Cr**	**Pd**			**W**	**Pt**
Energy [eV]	285.0	286.7	289.1	400.3	402.3	533.3	199.8	574.6	336.4	338.5	345.6	36.5	73.4
Chemical species	C-C	C-O-C C-OH C-N	O=C-O N-C=O	N-C. N-C=O	NH_4^+	O-Me. O=C/O-C	Cl- in e.g. $PdCl/PtCl_2$	Cr^0	PdO	$PdCl_2$	Pd_{loss}	WO 3	$PtO/PtCl_2$
Pt^{Os}NCs synthesized by **FLA-dc-APGD**	28.7	6.1	2.0	0.4	1.9	12.8	27.9	1.4	3.4	8.5	0.5	0.7	5.8
Pt^{Os}NCs synthesized by **FLC-dc-APGD**	33.4	8.5	3.3	0.6	0.7	11.1	25.2	1.7	0.0	0.0	0.0	0.0	15.6

256 **Table S5**. Surface compositions (atomic %) determined by fitting XPS spectra for $Os^{Pd/Cr}$NCs synthesized by FLA-dc-APGD and FLC-dc-APGD.

Element	**C**			**N**		**O**	**Mg**	**Si**		**P**	**Cl**	**Ca**	**Pd**		**Re**			**Os**
Energy [eV]	285.0	286.7	289.3	400.4	402.3	532.6	1304.3	99.3	103.1	133.7	198.6	348.2	338	339.8	43.5	44.6	46.4	53.6
Chemical species	C-C	C-O C-N	O=C-O N-C=O	N-C N-C=O	NH_4^+	O-Si. O-P O-Re. O-Pd O=C/O-C	Mg^{2+} in $MgCl_2$	Si^0	SiO_2	PO_4^{3-}	Cl^- in $MgCl_2$. $OsCl_3$. $CaCl_2$. $PdCl_2$	Ca^{2+} in $CaCl_2$	PdO_2/ $PdCl_2$	$PdCl_6$/ $Pd(NH_3)_4Cl_2$	ReO_2	ReO_3/ $ReCl_6$	Re_2O_7	$OsCl_3$/ OsO_2
$Os^{Pd/Cr}$NCs synthesized by **FLA-dc-APGD**	14.1	4.4	0.9	1.2	2.1	34.9	1.7	21.6	7.8	2.8	6.5	0.2	0.7	0.2	0.08	0.13	0.22	0.60
$Os^{Pd/Cr}$NCs synthesized by **FLC-dc-APGD**	24.3	14.7	5.5	3.5	3.1	30.9	1.3	2.8	4.8	0.4	6.5	0.0	0.4	0.3	0.19	0.33	0.66	0.43

257

Table S6. Surface compositions (atomic %) determined by fitting XPS spectra for $Ru^{W}NCs$ synthesized by FLA-dc-APGD and FLC-dc-APGD.

Element	**C**			**N**		**O**		**Si**		**Cl**			**Ru**	
Energy [eV]	285.0	288.0	290.7	400.1	401.7	531.3	533.1	99.8	103.6	197.9	198.9	200.2	463.8	465.6
Chemical species	C-C	C=O O-C-O	O-(C=O)-O	N-C	NH_4^+	O-Ru O=C	O-Si O-C OH	Si^0	SiO_2	Cl^- in e.g. $RuCl_2$	Cl^- in e.g. $RuCl_3$	Cx-Cl	$RuCl_2$/ RuO_2	$RuCl_3$
$Ru^{W}NCs$ synthesized by **FLA-dc-APGD**	37.4	7.3	2.1	0.8	1.0	6.8	16.4	0.0	3.9	6.1	7.9	1.4	7.6	1.4
$Ru^{W}NCs$ synthesized by **FLC-dc-APGD**	34.8	7.2	1.3	0.9	0.9	4.7	24.9	1.3	8.4	4.5	4.5	1.3	4.4	1.0

Table S7. Surface compositions (atomic %) determined by fitting XPS spectra for $W^{Ru/Os}$NCs synthesized by FLC-dc-APGD.

Element	**C**				**N**	**O**		**Na**	**S**	**Cl**		**W**
Energy [eV]	285.0	286.2	287.9	289.3	398.9	531.0	532.4	1072.1	168.8	198.7	200.2	35.5
Chemical species	C-C	C-OH C-O-C C-N C-Cl	C=O	O=C-O	N-C	O=C SO_4^{2-}	O-C OH	Na^+ in e.g. NaCl Na_2SO_4	SO_4^{2-} in e.g. Na_2SO_4	Cl^- in e.g. NaCl	C- Cl_3	W^{6+}
$W^{Ru/Os}$NCs synthesized by **FLC-dc-APGD**	13.9	4.5	2.2	1.7	0.4	3.4	2.1	41.8	0.3	21.1	8.4	0.3

Table S8. Surface compositions (atomic %) determined by fitting XPS spectra for Re^{Os}NCs synthesized by FLA-dc-APGD.

Element	**C**				**N**	**O**		**Na**	**S**	**Cl**		**W**
Energy [eV]	285.0	286.2	287.9	289.3	398.9	531.0	532.4	1072.1	168.8	198.7	200.2	35.5
Chemical species	C-C	C-OH C-O-C C-N C-Cl	C=O	O=C-O	N-C	O=C SO_4^{2-}	O-C OH	Na^+ in e.g. NaCl Na_2SO_4	SO_4^{2-} in e.g. Na_2SO_4	Cl^- in e.g. NaCl	C- Cl_3	W^{6+}
Re^{Os}NCs synthesized by **FLA-dc-APGD**	13.8	6.2	1.8	1.5	0.3	2.0	2.5	41.5	0.5	22.7	7.2	0.0

References

1 M. A. Khan, P. Cyganowski, P. Pohl, P. Jamroz, W. Tylus, A. Motyka-Pomagruk and A. Dzimitrowicz, *Colloids Surf. A Physicochem. Eng. Asp.*, 2024, **695**, 134190.

2 M. Müller, M. Dworschak, J. Benedikt and L. Kienle, *Particle & Particle Systems Characterization*, 2024, **41**, 2400037.

3 M. Dworschak, N. Kohlmann, F. Matějka, P. Galář, L. Kienle, J. Schäfer and J. Benedikt, *Plasma Processes and Polymers*, 2023, **20**, 2200129.

4 M. Cui, F. Wang, W. Zhao, D. Zhang, R. Liang, Q. Ou and S. Zhang, *Chemical Engineering Journal*, 2023, **460**, 141676.

5 A. Pitto-Barry, L. M. A. Perdigao, M. Walker, J. Lawrence, G. Costantini, P. J. Sadler and N. P. E. Barry, *Dalton Transactions*, 2015, **44**, 20308–20311.

6 E. S. Gnanakumar, W. Ng, B. Coşkuner Filiz, G. Rothenberg, S. Wang, H. Xu, L. Pastor-Pérez, M. M. Pastor-Blas, A. Sepúlveda-Escribano, N. Yan and N. R. Shiju, *ChemCatChem*, 2017, **9**, 4159–4163.

7 A. M. Ahadi, A. Hinz, O. Polonskyi, T. Trottenberg, T. Strunskus, H. Kersten and F. Faupel, *Journal of Vacuum Science & Technology A: Vacuum, Surfaces, and Films*, 2016, **34**, 021301.

8 V. Vekselman, Y. Raitses and M. N. Shneider, *Phys. Rev. E*, 2019, **99**, 063205.

9 S. M. Kim, G. S. Kim and S. Y. Lee, *Mater. Lett.*, 2008, **62**, 4354–4356.

10 S. Kohsakowski, F. Seiser, J. P. Wiederrecht, S. Reichenberger, T. Vinnay, S. Barcikowski and G. Marzun, *Nanotechnology*, 2019, **31**, 095603.

11 V. R. Chelli and A. K. Golder, *Journal of Chemical Technology and Biotechnology*, 2019, **94**, 911–918.

12 W. N. El-Sayed, J. Alkabli, R. F. M. Elshaarawy and Y. A. Hassan, *Arabian Journal of Chemistry*, 2024, **17**, 105655.

13 D. V. Francis, T. Aiswarya and T. Gokhale, *Heliyon*, 2022, **8**, e10640.

14 A. Sonawane, M. A. Mujawar and S. Bhansali, *Nanotechnology*, 2020, **31**, 365706.

15 J. D. Clogston and A. K. Patri, *Methods in Molecular Biology*, 2011, **697**, 63–70.

16 K. H. Santos, J. A. Ferreira, D. Osiro, R. A. de Carvalho, L. Alberto Colnago, C. Alves Júnior and E. Maria de Jesus Agnolon Pallone, *Appl. Surf. Sci.*, 2020, **531**, 147206.

17 Y. Zhao, A. Tao, Z. Chen, Y. Ruan, K. Wang, L. Zhu and L. Chen, *Plasma Science and Technology*, 2025, **27**, 035505.

18 N. A. Sirotkin, A. V. Khlyustova, V. A. Titov, A. S. Krayev, D. I. Nikitin, O. A. Dmitrieva and A. V. Agafonov, *Plasma Chemistry and Plasma Processing*, 2020, **40**, 571–587.

19 K. S. Wong, N. S. L. Chew, M. Low and M. K. Tan, *Processes*, 2023, **11**, 2213.

20 M. Zhianmanesh, A. Gilmour, M. M. M. Bilek and B. Akhavan, *Appl. Phys. Rev.*, 2023, **10**, 21301.